Variational Shape Representation for Modeling, Elastic Registration and Segmentation

Amal A. Farag, Ahmed Shalaby, Hossam Abd El Munim and Aly Farag

Abstract Shapes describe objects in terms of information invariant to scale, translation and rotation. Depending of the data source, shapes may be represented by object contours or representation/transformations that sustain the objects characteristics, such as the signed distance function. Biomedical objects have inherent plasticity due to movement and changes over time. Elastic registration is a fundamental image analysis step for tracking anatomical structures, diseases, progress of treatment and in image-guided interventions. Variational level set methods (LSM) represent objects' contours through an implicit function that enables tracking the objects' topologies. This chapter provides an overview of variational shape modeling as applied to the registration and segmentation problems. The chapter evaluates similarity/dissimilarity measures and common energy functional representations used in elastic shape registration. Common numerical methods to solve the optimization involved are studied. In addition, the chapter discusses clinical applications for which shape-based models enable robust performance with respect to occlusion and other image degradation.

A. A. Farag (✉)
Imaging Biomarkers and Computer-Aided Diagnosis Laboratory, NIH, Bethesda, MD, USA
e-mail: aly.farag@louisville.edu

A. Shalaby · A. Farag
Department of Electrical and Computer Engineering, University of Louisville, Louisville, KY, USA
e-mail: www.cvip.uofl.edu

H. Abd El Munim
Computer and Systems Engineering Department, Ain Shams University, Cairo, Egypt
e-mail: hossamabdelmunim@gmail.com

S. Li and J. M. R. S. Tavares (eds.), *Shape Analysis in Medical Image Analysis*, Lecture Notes in Computational Vision and Biomechanics 14,
DOI: 10.1007/978-3-319-03813-1_3,

1 Introduction

In this chapter, we summarize and expand upon our work on variational shape modeling for segmentation and registration (e.g., [1–10]). Specifically, we represent shapes using vector distance functions (VDF). We use the VDF as shape prior for both shape-based segmentation and elastic shape registration. We derive the energy formulation for elastic registration and shape-based segmentation. We highlight the algorithms and the optimization technique used for solving the energy function. Finally, we apply the methodologies for various biomedical image analysis problems.

Shapes are represented either explicitly or implicitly [1, 9]. 2D/3D shape boundary points can be used directly/explicitly to deal with shapes (e.g., applications of alignment and retrieval) where the shape points are used directly to compute shape geometric properties and features. In the implicit shape representation, the shape boundary points can be computed by solving the zero level equation of the implicit shape function. This representation can be in either scalar or vector form. In this chapter, we use the VDF shape representation as a similarity measure in the shape registration process. More general transformations with inhomogeneous scaling, rotation, and translation parameters will be incorporated. The use of such vector functions results in a more adequate energy function which is optimized to achieve the transformation parameters both in the global and local registration schemes. A variational framework for the registration process is formulated. The gradient descent optimization criterion is used to handle the global registration similar to that in [11]. The local deformations are covered using the incremental free form deformations. The gradient descent optimization is not used to estimate the positions of the control points where the number of deformation parameters are large compared to the global alignment case. We demonstrate the nonrigid registration problem in vector implicit spaces as well.

Following our latest results (e.g., [9, 10]), we adopt a closed form solution for computing the elastic registration parameters which provides a large time reduction in comparison to the large number of iterations required by the gradient descent approach. We propose a quadratic energy function in terms of the control points positions (i.e., unknowns). Hence, the objective function is convex which leads to a single point solution of the minimization problem. Different experimental results for synthetic and real shapes registration cases will be demonstrated to show the efficiency of the proposed techniques. Also, comparison with the state of the art approaches will be discussed in detail.

The treatment below on shape representation and registration is based on our work [10]. We keep similar notations as well. Later on in the chapter we expand on this work for simultaneous segmentation and registartion of objects using shape priors.

2 Shape Representation

A map, $\mathbf{C}(p) : [0, 1] \subset R \rightarrow R^2$ defines a planar smooth curve with parameter p. The cartesian coordinates of the point vector can be defined by $\mathbf{C}(p) = [x(p)y(p)]^T$ where $0 \leq p \leq 1, 0 \leq x, \leq X$ and $0 \leq y, \leq Y$. This is the explicit representation of the given shape or contour $\mathbf{C}$. Open shapes have the relation $\mathbf{C}(0) \neq \mathbf{C}(1)$. A closed contour will always have $\mathbf{C}(0) = \mathbf{C}(1)$. Parameterizing complicated topology shapes is a challenge which is considered a disadvantage of the explicit shape representation method. Thus, a parametrization-free representation is needed. The implicit shape representation satisfies this condition as shown.

Given a smooth curve $\mathbf{C}^\alpha$ (defined above), that represents boundaries of the shape of interest, the following implicit vector function is defined as $\Phi_\alpha(\mathbf{X}) : \Omega_\alpha \subset \mathbf{R^2} \rightarrow \mathbf{R^2}$ where

$$\Phi\alpha(\mathbf{X}) = \mathbf{X}_0 - \mathbf{X} = [\phi_1\phi_2]^T, \mathbf{X} \in \Omega_\alpha, \phi_1 \; and \; \phi_2 \in R, \tag{1}$$

where $\mathbf{X}_0$ is the point on $\mathbf{C}^\alpha$ with the minimum Euclidean distance to $\mathbf{X}$ where $\mathbf{X} \in \Omega_\alpha$ (Ω_α is the domain that includes the shape/contour). The surface or boundary points always satisfy the relation $||\Phi_\alpha(\mathbf{C}^\alpha)|| = 0$. Note, that the implicit representation is dependent only on the boundary position, not on any parameterizations, and hence, it is suitable to represent a cloud of points or even scattered edge boundaries.

If a global transformation is applied to the given shape represented by the designed vector map, one can predict the map of the new shape. We define a shape β that is obtained by applying a transformation $\mathbf{A}$ to a given shape α. Let us assume that the transformation has a scale matrix $\mathbf{S}$, a rotation matrix $\mathbf{R}$, and a translation vector $\mathbf{T}$. The transformation can be written for any point $\mathbf{X}$ in the space as $\mathbf{A} = \mathbf{SRX} + \mathbf{T}$.

Applying the transformation to the given points results in the pair of points $\hat{\mathbf{X}}$, $\hat{\mathbf{X}}_0 \in \Omega_\beta$ (Domain of the Target Shape where $\Omega_\beta \subset R^2$). It is straightforward to show that:

$$\Phi_\beta(\mathbf{A}) = \hat{\mathbf{X}}_0 - \hat{\mathbf{X}} = \mathbf{SR}(\mathbf{X}_0 - \mathbf{X}) \tag{2}$$

as such the following relation holds:

$$\Phi_\beta(\mathbf{A}) = \mathbf{SR}\Phi_\alpha(\mathbf{X}) \tag{3}$$

Which illustrates that this representation can give a vector similarity measure that includes inhomogeneous scales and rotations. Also, it is invariant to the translation parameters, while the effect of scales and rotations can be predicted. This measure overcomes the problem of using the conventional signed distance maps that leads to the use of homogeneous scales only. Note, that the VDF components are smooth and differentiable at the boundary points.

3 Global Registration of Shapes

Finding point-wise correspondences (between the two given source and target shapes defined respectively by $\mathbf{C}^{\alpha}$ and $\mathbf{C}^{\beta}$) is the objective of the registration problem. An energy function is built based on the vector dissimilarity measure. The VDF shape representation changes the problem from the shape boundary domain to the higher dimensional vector representation. A transformation, $\mathbf{A}$, that gives pixel-wise vector correspondences between the two shape representations Φ_{α} and Φ_{β}, is required to be estimated.The problem now can be considered as a global optimization that includes all points in the image domain. Sum of squared differences will be considered with energy optimized by the gradient descent approach.

According to the properties of the implicit vector representation shown, the following dissimilarity measure is used: $\mathbf{r} = \mathbf{SR}\Phi_{\alpha}(\mathbf{X}) - \Phi_{\beta}(\mathbf{A})$ and the optimization energy function is formulated by the sum of squared differences as: $E(\mathbf{S}, \mathbf{R}, \mathbf{T}) = \int_{\Omega\alpha} \mathbf{r}^T \mathbf{r} d\Omega_{\alpha}$. The complexity of the problem is reduced by considering only points around the zero level of the vector function and neglecting mapping of far away points. The matching space is limited to a small band around the surface that can be selected by introducing the following energy function:

$$E(\mathbf{S}, \mathbf{R}, \mathbf{T}) = \int_{\Omega\alpha} \delta_{\varepsilon}(\Phi_{\alpha}, \Phi_{\beta}) \mathbf{r}^T \mathbf{r} d\Omega_{\alpha}. \tag{4}$$

where $\delta_{\varepsilon}$is an indicator function defined in [1].
The optimization of the given criterion is handled using the gradient descent method:

$$\frac{d}{dt}\vartheta = 2 \int_{\Omega\alpha} \delta_{\varepsilon} \mathbf{r}^T [\nabla_{\vartheta}(\mathbf{SR}\Phi_{\alpha}(\mathbf{X})) - \nabla\Phi_{\beta}^T(\mathbf{A})\nabla_{\vartheta}\mathbf{A}] d\Omega_{\alpha} \tag{5}$$

where $\vartheta \in \{S_x, S_y, \theta, T_x, T_y\}$ represents the set of scale, rotation, and translation parameters respectively.

3.1 Evaluation of Global Registration

In [10] we reported results for an experiment that involved 100 registration cases, using the corpus callosum (simple shape) and the hippocampus (four separate parts). Each case considers a source and a target shape. The source is fixed and the target is generated by applying a transformation on the source. Parameters $(S_x, S_y, \theta, T_x, T_y)$ are created and selected randomly from the ranges [0.8, 1.2], [0.8, 1.2], $[-60°, 60°]$, $[-60, 60]$ respectively. These generated patterns are kept as the ground truth for each case. The gradient descent optimization is performed to obtain a steady state estimate for each parameter associated with each registration case. The algorithm shows successful results for the one hundred cases and the energy decreases smoothly with the increase of the iteration number until perfect alignment is achieved. The measurements show that the mean errors and standard deviations (Table 1) are very

Table 1 Mean error (μ) and its standard deviation (δ) for the transformation parameters of the corpus callosum (CC) and hippocampus (HC) cases ($\mu \pm \delta$)

Structure	S_x	S_y	θ°	T_x	T_y
CC	-0.005 ± 0.009	-0.003 ± 0.007	-0.002 ± 0.018	-0.5 ± 0.4	-0.3 ± 0.5
HC	0.009 ± 0.007	0.005 ± 0.004	0.001 ± 0.09	0.00 ± 0.02	-0.0 ± 0.02

Parameter ranges:[0.8, 1.2], [0.8, 1.2], [$-60°$, $60°$], [-60, 60], [-60, 60], are used

appropriate and satisfactorily small. The final registration emphasizes that for each experiment, the boundaries of the source and target shapes become very close to one another. The gradient descent successfully estimates the scales, rotations, and translations with proper initialization.

In addition, we formed three groups of different shapes (Fighter Jet, Fishes, Number Four). Each group includes 11 instances of its corresponding shape. Different global registration processes are conducted by randomly taking 11 pairs from each group. For each pair of shapes, the correlation coefficient is calculated to measure the similarity between the shape representations: $\gamma = \frac{E[(||\Phi_\alpha||-\mu_\alpha)(||\Phi_\beta||-\mu_\beta)]}{\sigma_\alpha \sigma_\beta}$ where μ, σ stand for mean and standard deviation of the shape vector representations magnitudes respectively. The global registration process successfully increases the coefficient dramatically. Before alignment, the mean correlation coefficients and their standard deviations for the groups are (0.836 ± 0.047), (0.834 ± 0.087), and (0.754 ± 0.092), respectively. After alignment, the coefficients become (0.969 ± 0.013), (0.953 ± 0.03), and (0.911 ± 0.039). Note, that the last group has the largest local shape variations and hence, has the smallest average coefficient 0.911, which is small compared to other groups of coefficients.

For comparison with other techniques, two synthetic shape images have been created. The second image results by stretching the first with large inhomogeneous scales ($S_x = 2.5$, $S_y = 3.3$). Mutual information is used to register these contours (images) according to the technique in [15]. Mutual information suffers in such a situation because the scale range will increase/decrease the energy in one direction, providing unacceptable results (minimum position does not provide the correct parameters as shown in Fig. 1 left image). The proposed approach aims to align the contours of the given images to each other to obtain a global minimum at these scales exactly as shown, which is considered to be an advantage over the mutual information.

3.2 Global Registartion for Segmentation of Lung Nodule Regions

We use the global alignment approach with the shape-based segmentation as an application. In our previous work [2], we formulated the problem as a global registration between a shape and an intensity model implicit representation. In this paper, we adopt the above alignment technique to segment lung nodule regions [16]. Nodule size is an important factor in volumetric analysis of lung nodules. It has been

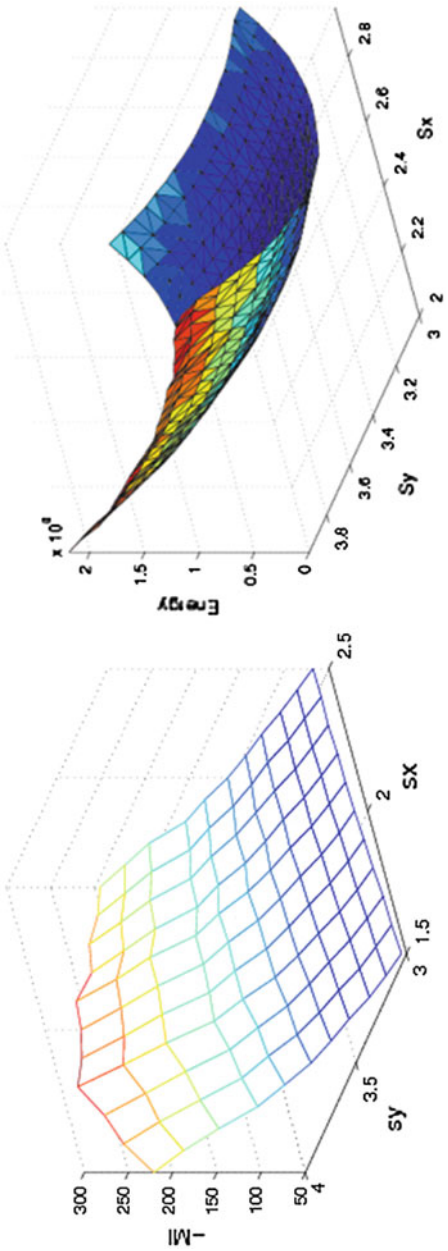

Fig. 1 Large scales registration case: the negative of mutual information is given to the *left*. The proposed energy is given to the *right*. The mutual information and the proposed energy are shown as functions of and the proposed energy are shown as functions of S_x and S_y

shown clinically that size is linked to nodule malignancy, with non-calcified nodules larger than in diameter having a higher rate of malignancy than smaller nodules. Size computation is usually performed by applying volumetric methods to a segmentation result. However, lung nodules segmentation in CT imaging is a complex and challenging process. One of the most important problems arises from possible attachments of the nodules to other anatomical objects. The lungs are a complex anatomical structure. Vessels, fissures, bronchi or pleura are structures that can be located close to lung nodules.

From our experience, we noticed that the main nodule regions considered for size computation are elliptic. A circle model is represented implicitly by the vector function Φ_p. A region of interest image (ROI) is taken from the whole lung CT scan to include the nodule. Intensity segmentation of the ROI is represented implicitly by the vector function Φ_g. Aligning the two models using the above approach will result in an ellipse that includes the nodule region. The model is initialized and then the alignment parameters are estimated using the gradient descent optimization. Different scales, rotation, and translation parameters are computed in each case to obtain an ellipse exactly around the nodule (see Fig. 2). The ellipse axis rotates while its size changes to include the boundaries of the nodule. A thresholding technique can be used later to remove the non-nodule parts from the elliptic areas.

4 The Elastic Registration Problem

Our objective is to find a function that gives the point correspondences between the two given domains (source and target). Let us define the $2D$ shape elastic registration as follows:A map $\mathbf{C}^{\hat{\alpha}}(\tau_s) : [0, 1] \in R \rightarrow R^2$ defines a planar source curve with a parameter τ_s (it is the source shape $\mathbf{C}^{\alpha}$ after applying the global transformation estimated by the methods above). The target is defined by $\mathbf{C}^{\beta}(\tau_t) : [0, 1] \in R \rightarrow R^2$. Assume that $\mathbf{C}^{\hat{\alpha}}(\tau_s)$ is the corresponding point of $\mathbf{C}^{\beta}(\tau_t)$ (the criteria for finding the correspondences can be found in the following sections). The output will be a C^0 function $f : R^2 \rightarrow R^2$ with $f(\mathbf{C}^{\hat{\alpha}}(\tau_s)) = \mathbf{C}^{\beta}(\tau_t)$. Different interpolation functions have been proposed to handle this problem [12]. We choose the free form deformation *FFD* model, based on B-splines [13, 14], which is a powerful tool for modeling deformable objects and has been previously applied to the tracking and motion analysis problems. The basic idea is to deform the shape by manipulating a mesh of control points. The resulting deformation controls the shape of the object and produces a smooth and continuous transformation.

Consider an $M \times N$ lattice of control points $\mathbf{P} = \mathbf{P}_{m,n}; m \in \{1, \ldots, M\}; n \in \{1, \ldots, N\}$, each point on the source shape will have the following form of deformation:

$$\mathbf{L}(\tau_s) = \sum_{k=0}^{3} \sum_{l=0}^{3} B_k(u) B_l(v) \delta \mathbf{P}_{i+k, j+1} \tag{6}$$

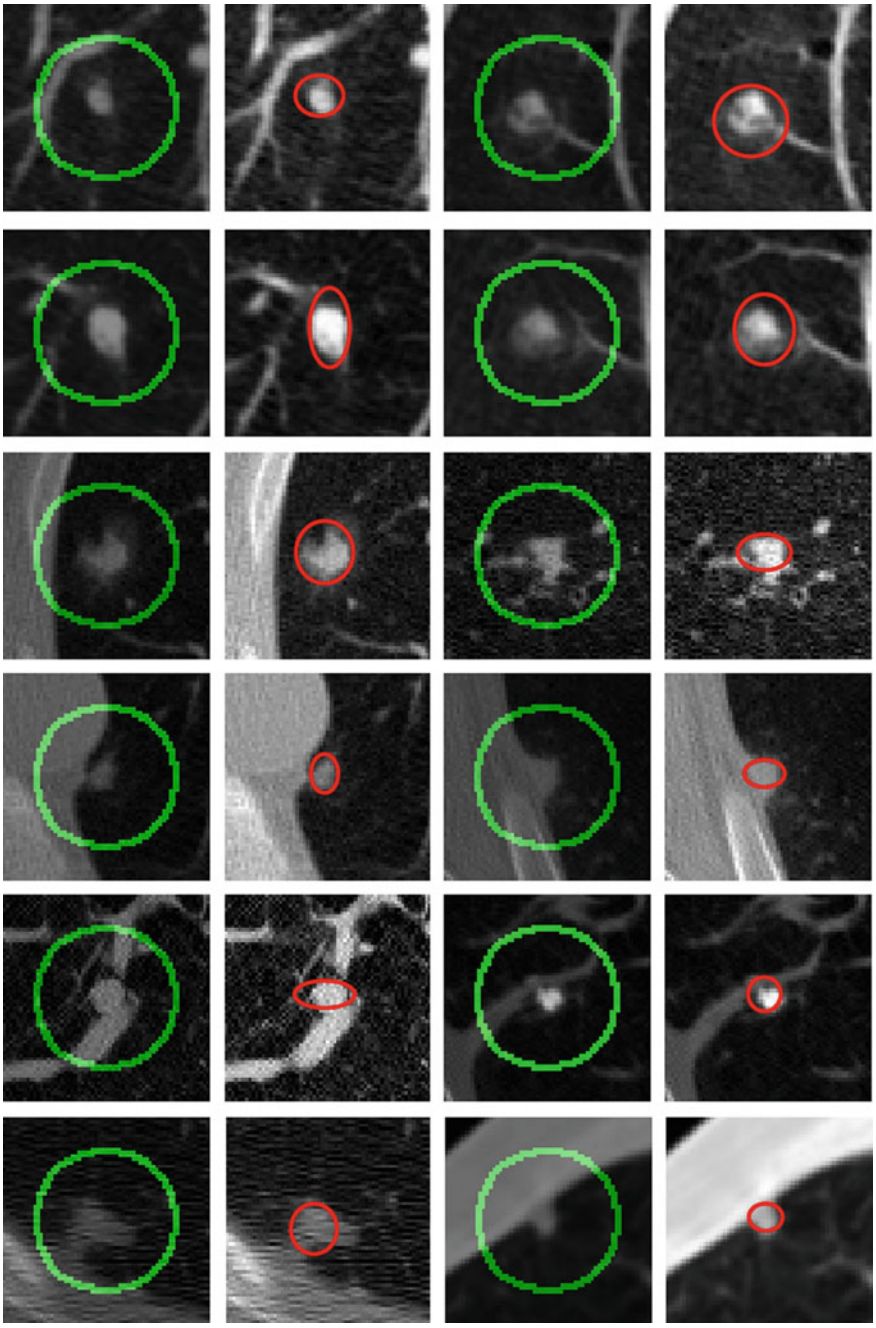

Fig. 2 Initial positions are shown in *green* at the first and third columns while final ellipses are demonstrated in *red* at the second and fourth columns

where $\delta\mathbf{P} = \delta\mathbf{P}_{m,n} \in \{[\delta\mathbf{P}^x_{1,1}\delta\mathbf{P}^y_{1,1}]^T, \ldots, [\delta\mathbf{P}^x_{M,N}\delta\mathbf{P}^y_{M,N}]^T\}$ is the control point deformation vector, $i = (x.(M-1)/X)+1$, $j = (y.(N-1)/Y)+1$, $u = x.M/X)$, $v = y.N/Y - (y.N/Y)$, and the spline basis functions (B) are defined in [14]. So the cubic B-spline is used as an approximation function for our interpolation problem. Below, we propose and discuss the problem solution in implicit and explicit spaces. In [10], we devised a closed form solution of the interpolation function parameters.

4.1 A Coarse to Fine Strategy with IFFD's

The control lattice points are required to move to correctly obtain correspondences over shape boundaries. A very small error can be achieved when using a high resolution control lattice since the number of degrees of freedom increases. However, this is not enough. Such sudden movement will result in unnecessary cross overs of the domain grid lines and the registration process will be meaningless. This will result in changing and corrupting the object topology. A better way is to move the grid step by step towards the target.

To avoid this, a coarse to fine strategy is used (equivalent to the incremental free form deformations used in [15]). We start with a resolution of 4×4 and solve for the deformation. Iteratively we increase the resolution to 5×5, 6×6, and so on and so forth. In each step, the positions of the control points are computed and the contour moved to the new position until a satisfactory error distance is obtained. The result is smooth and the correspondence is achieved accurately. This process handles the error extremely well and provides an impressive infinitesimal energy function and smooth grid deformations simultaneously.

4.2 Solution in Vector Implicit Spaces

Following the work in [11], a local deformation vector $\mathbf{L} = \mathbf{L}(\mathbf{X}) = \mathbf{L}(\delta\mathbf{P})$(described above) is applied to the globally transformed shape represented by $\hat{\alpha}$. The following dissimilarity measure is considered:

$$\mathbf{r}_n - \Phi_{\hat{\alpha}}(\mathbf{X}) - \Phi_{\beta}(\mathbf{X} + \mathbf{L}) \tag{7}$$

and hence the non rigid energy function will be defined as:

$$E^{\Phi}_n(\delta\mathbf{P}) = \int_{\Omega_{\hat{\alpha}}} \mathbf{r}^T_n \mathbf{r}_n d\Omega_{\hat{\alpha}} \tag{8}$$

The local deformations are smoothed by adding another term that includes their derivatives as follows:

$$E_n^{\Phi}(\delta\mathbf{P}) = \int_{\Omega_{\hat{\alpha}}} \mathbf{r}_n^T \mathbf{r}_n d\Omega_{\hat{\alpha}} + \lambda \int_{\Omega_{\hat{\alpha}}} (||\mathbf{L}_x||^2 + ||\mathbf{L}_y||^2 + ||\mathbf{L}_{xx}||^2 + ||\mathbf{L}_{yy}||^2) d\Omega_{\hat{\alpha}} \quad (9)$$

As an interpretation, the energy contains a term for covering the local deformations and another for penalizing large derivatives. To make the addition homogeneous, we weight the second term by $\lambda \in R^+$. Again, we take the derivative of the energy with respect to each of the unknown parameters as follows:

$$\frac{\partial E_n^{\Phi}}{\partial \delta\mathbf{P}} = -2 \int_{\Omega_{\hat{\alpha}}} \mathbf{r}_n^T (\nabla\Phi_\beta)^T \frac{\partial \mathbf{L}}{\partial \delta\mathbf{P}} d\Omega_{\hat{\alpha}} + 2\lambda \int_{\Omega_{\hat{\alpha}}} ((\mathbf{L}_x)^T \frac{\partial \mathbf{L}_x}{\partial \delta\mathbf{P}} + (\mathbf{L}_y)^T \frac{\partial \mathbf{L}_y}{\partial \delta\mathbf{P}} + (\mathbf{L}_{xx})^T \frac{\partial \mathbf{L}_{xx}}{\partial \delta\mathbf{P}} + (\mathbf{L}_{yy})^T \frac{\partial \mathbf{L}_{yy}}{\partial \delta\mathbf{P}}) d\Omega_{\hat{\alpha}} \quad (10)$$

We assume that the amount of pixel deformation is relatively small such that its vector representation can be approximated using Taylor series expansion as: $\Phi_\beta(\mathbf{X}+\mathbf{L}) \approx \Phi_\beta(\mathbf{X}) + (\nabla\Phi_\beta(\mathbf{X})^T)\mathbf{L}$. The control points are required to move and minimize the above objective function and hence satisfy the following zero condition: $\frac{\partial E_n^{\Phi}}{\partial \delta\mathbf{P}} = [0 \quad 0]^T$. By setting $\Phi(\mathbf{X}) = \Phi_{\hat{\alpha}}(\mathbf{X}) - \Phi_\beta(\mathbf{X})$, the above formulation will lead to:

$$\int_{\Omega_{\hat{\alpha}}} \Phi^T (\nabla\Phi_\beta)^T \frac{\partial \mathbf{L}}{\partial \delta\mathbf{P}} d\Omega_{\hat{a}} = \int_{\Omega_{\hat{\alpha}}} ((\nabla\Phi_\beta)^T \mathbf{L})^T (\nabla\Phi_\beta)^T \frac{\partial \mathbf{L}}{\partial \delta\mathbf{P}} d\Omega_{\hat{a}} + \lambda \int_{\Omega_{\hat{\alpha}}} ((\mathbf{L}_x)^T \frac{\partial \mathbf{L}_x}{\partial \delta\mathbf{P}} + (\mathbf{L}_y)^T \frac{\partial \mathbf{L}_y}{\partial \delta\mathbf{P}} + (\mathbf{L}_{xx})^T \frac{\partial \mathbf{L}_{xx}}{\partial \delta\mathbf{P}} + (\mathbf{L}_{yy})^T \frac{\partial \mathbf{L}_{xx}}{\partial \delta\mathbf{P}}) d\Omega_{\hat{a}} \quad (11)$$

Fortunately, the above equation is linear in terms of control points deformations. We can formulate the following linear system to give a closed form solution for the unknown deformations:

$$\bar{\mathbf{\Psi}}\mathbf{\Theta} = \bar{\mathbf{\Lambda}} \quad (12)$$

where:

$$\bar{\Psi}_{r,c} = \int_{\Omega_{\hat{\alpha}}} ((\nabla\Phi_\beta)^T \mathbf{L}^{r,c})^T (\nabla\Phi_\beta)^T \frac{\partial \mathbf{L}}{\partial \theta_r} d\Omega_{\hat{\alpha}} + \lambda \int_{\Omega_{\hat{\alpha}}} ((\mathbf{L}_x^{r,c})^T \frac{\partial \mathbf{L}_x}{\partial \theta_r} + (\mathbf{L}_y^{r,c})^T \frac{\partial \mathbf{L}^y}{\partial \theta_r} + (\mathbf{L}_{xx}^{r,c})^T \frac{\partial \mathbf{L}_{xx}}{\partial \theta_r} + (\mathbf{L}_{yy}^{r,c})^T \frac{\partial \mathbf{L}_{yy}}{\partial \theta_r}) d\Omega_{\hat{\alpha}}, \quad (13)$$

$$\bar{\Lambda}_r = \int_{\Omega_{\hat{\alpha}}} \Phi^T (\nabla\Phi_\beta)^T \frac{\partial \mathbf{L}}{\partial \theta_r} d\Omega_{\hat{\alpha}}. \quad (14)$$

Note, that this will lead to computing new positions of the control lattice points and hence, we can compute the entire domain deformation field. Other approaches use gradient descent to compute the position of each point in space. Unfortunately, the use of this form of local deformation does not guarantee proper handling of the registered shape since it cannot preserve topology. Also, it results in scattered front points leading to an open surface which is not the case. Another issue is that the gradient descent does not guarantee the desired solution especially when using a large number of deformation vectors.

Now we will illustrate the whole algorithm for elastic shape registration in vector implicit spaces. Assume that $N_x^i \times N_y^i$ is the resolution of the control lattice initially denoted by i. The resolution at any time will be $N_x \times N_y$. The basic algorithm steps are shown as follows:

1. Set $N_x = N_x^i$ and $N_y = N_y^i$ (initial grid size).
2. Compute the vector distance representation of the source and target shapes $\Phi_{\hat{\alpha}}$ and Φ_β respectively.
3. Construct a control lattice of size $N_x \times N_y$ and initialize its point deformation vectors to zeros.
4. Construct and Solve Eq. 12 to obtain the new deformation of each control point and hence, compute its new position.
5. Based on the new lattice, update the source points and its vector representation, $\Phi_{\hat{\alpha}}$, by computing the new deformation field using Eq. 6.
6. Set $N_x = N_x + 1$ and $N_y = N_y + 1$.
7. Check the stopping criteria. Either the objective function goes below a certain threshold or a number of maximum resolution levels is reached, otherwise go to step #3.

4.3 Evaluation

The point-based algorithm described in [8] looks simple and does not require huge space to store the shape representation. However, for many registration cases, we obtain unsatisfactory results. This is due to its use of the closest point criteria to decide the correspondences. Examples of shapes that show the failure of the algorithm are shown in Fig. 3. It is clear that these examples fail because the left end of the source shape arrives at the center line of the target. The decision to go left or right becomes very difficult since both directions have the same distance.The above algorithm works efficiently and handles the cases that the former algorithm fails to register as shown in last row of Fig. 3 (see also [10]).

The reason for the success is that the approach minimizes the differences between the two implicit representations and hence, makes the two contours very close to each other. The neighborhood vectors around the shape boundaries have small magnitudes. This property with the delta function described above helps in moving the contour smoothly in the proper direction. This creates a force that stretches the source to the

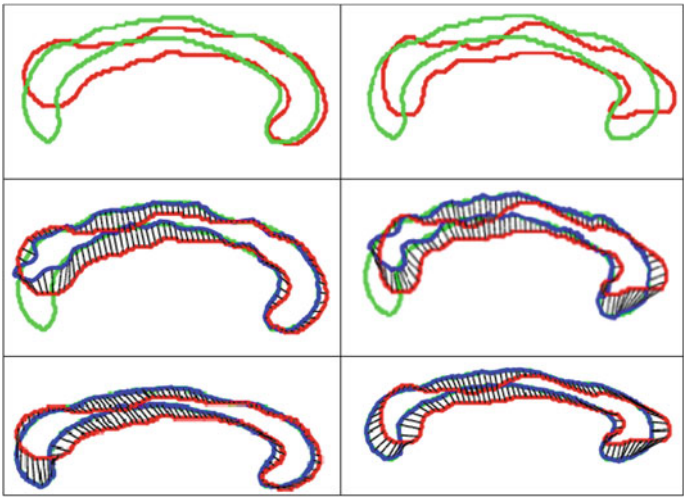

Fig. 3 Different elastic registration examples: source contour is given in *red*, target contour is drawn in *green*, and deformed contour is shown in *blue*. Initial contours are shown in the first row. The second row shows the failure of the ICP [16] algorithm with the IFFD given in [9]. The success of our approach is demonstrated in the last row

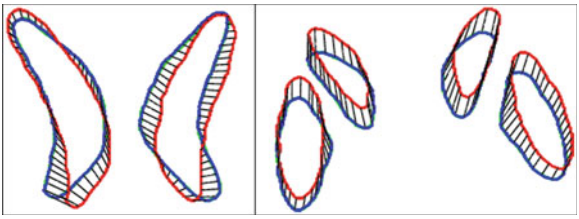

Fig. 4 Different elastic registration examples of shapes containing multiple parts using the implicit vector representation: source contour is given in *red* while target contour is drawn in *blue*. Correspondences for the ventricle is shown to the *left* while hippocampus results are illustrated to the *right*

target while the free form deformation preserves the topology of the shape. In all of the registration cases, we notice that the grid deformation is smooth and each grid line is kept in its order without crossovers or folding.

The algorithm works for multiple objects without any problem since it is not necessary to handle the parameterizations. Elastic registration cases of two-part and four-part shapes are illustrated in Fig. 4 for the brain ventricles and the hippocampus shapes.

For more validation of the above algorithm, a deformed shape is generated from a given tooth model. The target shape is generated by applying random deformations on the source image such that correspondences are stored as ground truth for validation. The model is from real data of a Cone-beamed Computed Tomography scan of resolution 0.2 mm per pixel (Fig. 5a).The approach is applied by increasing the

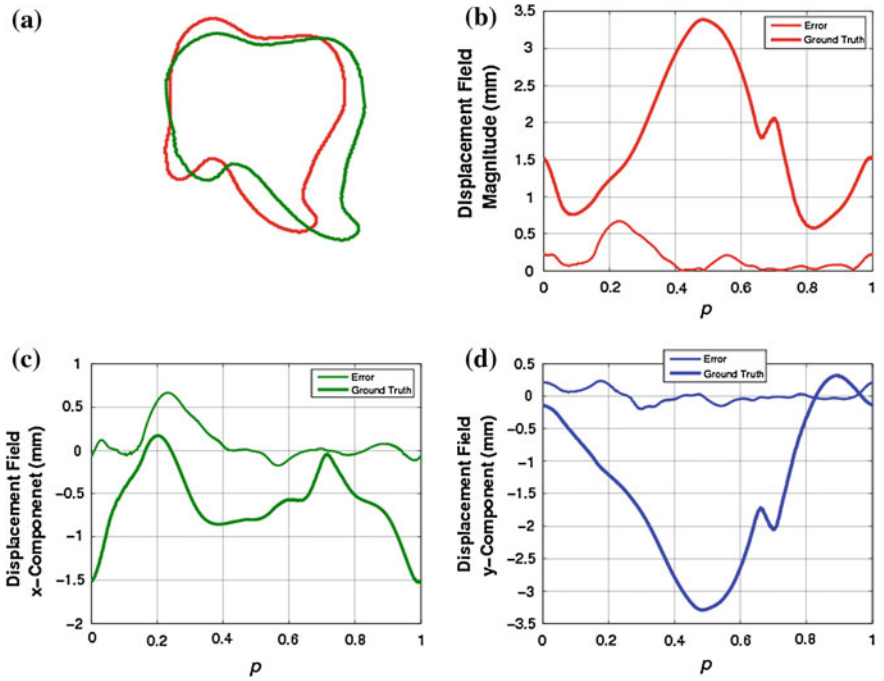

Fig. 5 A local registration example with displacement field measurements: **a** initial shape contours of the source and target models, **b** displacement field magnitude plot over the shape contour, **c** x-component of the displacement field error, and **d** y-component of the displacement field error

resolution of the control lattice one step in each direction at a time starting from a grid of 5×5. The contours come closer to each other iteratively until steady state is reached. The approach shows very high accuracy. The displacement field is achieved with an average error of 0.1677 mm. As shown in Fig. 5b–d, errors of the displacement fields are plotted versus the curve parameterizations allowing a follow up of the error distribution over the whole shape boundary.

Compared to the proposed in [15], the above algorithm is more complicated but the closed form solution for the control points positions possesses a great advantage. Also, if we do not use the closed form solution, the total execution time will be doubled. Assume that the registration problem needs N incremental levels of free form deformations, each level has, $N_{cp} = n_x \times n_y$ control points, and hence, $2 \times N_{cp}$ unknown variables x and y components for the gradient descent. If the average number of iterations of the gradient descent needed for each variable to reach the steady state is N_{Iter} with average time per iteration of Δt (with the method in [15]), the total time will be: $Time_1 = \sum_{i=1}^{N} (2 \times N_{CP}^i * N_{Iter} \times \Delta t)$. For the same IFFD setup with the gradient descent of Eq. 10 which does not use the closed form solution, the total time will be doubled; $Time_2 = \sum_{i=1}^{N} (2 \times N_{CP}^i \times N_{Iter} \times (2 \times \Delta t))$, since we use an implicit vector representation which has two components. The gradient descent execution time for an iteration will be roughly twice that of Δt. In the case of applying the proposed closed

form solution, the gradient descent iterations will be omitted. The new execution time can be estimated as: $OurTime = \sum_{i=1}^{N}(2 \times N_{CP}^{i} \times (2 \times \Delta t))$. The time to construct the linear system of the closed form (Eq. 12) is equal to the time of one gradient descent iteration for all variables. Our time holds the relation: $OurTime = 2 * Time_1/N_{Iter}$. A good steady state solution for the gradient descent needs a number of iterations greater than which guarantees that our execution time is less than that of the approach in [15].

5 Variational Shape-Based Segmentation

Variational approaches segment shapes through an energy minimization framework that controls the evolution of an implicit/explicit contour/surface. The active contour models proposed by Kass et al. [20] and level sets proposed by Osher and Sethian [19] are the most important variational methods in the literature. The active contour models minimize the energy formulation using the explicit shape representation, which requires parameterizations of the contour. Explicit shape representations suffer when applied to shape modeling since they do not allow the shape to undergo topological changes. The level sets method uses implicit shape representation, which does not need contour parameterizations, and handles the topological changes of shapes.

Tsai et al. [24] proposed a shape model using a signed distance function of the training data. The Eigenmodes of implicit shape representations are used to model the shape variability. They proposed a shape prior using a coefficient of each training shape. Cremers et al. [26] proposed a simultaneous kernel shape based segmentation algorithm with a dissimilarity measure and statistical shape priors. This method is validated using various image sets which objects are tracked successfully. In [15] the distance function is used to implicitly represent open/closed shapes (structures). The images of distance functions are registered using the mutual information approach. In addition to global registration, they used a b-spline based incremental Free Form Deformation (IFFD) to minimize a dissimilarity measure. Taron et al. [25] proposed an invariant representation of shapes, and computing uncertainties on the registration process. They proposed a dimensionality reduction technique to lower the cost of the density estimate computation of kernel based shape model. Mahmoodi [28] proposed a shape-based active contours for fast video segmentation. Their level sets implement is based on Mumford-Shah [29] and Chan-Vese [21] methods. They compared their method with only intensity based segmentation method.

5.1 Methods

The intensity (as the existing information) and shape (as the prior information) are modeled to obtain the optimum segmentation in this study. The intensity information is modeled using the histogram of gray levels of the image. This information is mod-

eled using the Gaussian distribution. The model estimates the marginal density for each class. Kendall [18], definesshape the geometrical information that remains when location, scale, and rotational effects are filtered out from an object. Hence, the shape information is modeled after the sample shapes are transformed into the reference space. The shape variability is modeled using the occurrences of the transformed shapes. To label the image into meaningful areas, the chosen information is modeled to fit progressively in each of the regions by an optimization process. Each pixel in the image will have two probabilities to be an object and a background class based on the intensity and shape models. These probabilistic values will guide the energy (cost) functionals in the optimization process. Next sections detail the proposed method

5.1.1 Generation of the Shape Prior

As described in [30], the shape model is required to capture the variations in the training set. This model is considered to be a weighted sum of the new projected SDFs's as follows:

$$\Phi_{\mathbf{P}} = \sum_{a=1}^{N} \omega_a \Phi_a^t \tag{15}$$

Let $\mathbf{W} = [\omega_1, \ldots, \omega_N]^t$ to be the weighting coefficient vector. By varying these weights, $\Phi_{\mathbf{P}}$ can cover all values of the training distance functions and, hence, the shape model changes according to all of the given images. A new probabilistic and dynamic shape model is synthesized using the first four principal components. Two shape probability density functions which represent the probability of i) the object (inside of a boundary) and ii) background regions (outside of a boundary) are obtained:

$$P_o^s(x) = \frac{\sum_{j=1}^{N} \omega_j |\Phi_j^t(x)| H(-\Phi_j^t(x))}{\sum_{j=1}^{N} \omega_j |\Phi_j^t(x)|}, P_b^s(x) \frac{\sum_{j=1}^{N} \omega_i |\Phi_j^t(x)| H(\Phi_j^t(x))}{\sum_{j=1}^{N} \omega_j |\Phi_j^t(x)|}, \tag{16}$$

where $H(.)$ is the Heaviside step function as a smoothed differentiable version of the unit step function. Also, we should note that $P_o^s(\mathbf{x}) + P_b^s(\mathbf{x}) = 1$. This step is integrated into the registration step which is described in section 5.1.2, hence the shape model is dynamically reconstructed in the registration process.

Figure 6 shows the detailed description of the shape model where the shape weighting coefficients are normalized, i.e. $\mathbf{w} = \{\omega_1, \ldots, \omega_N\} = \{1/N, \ldots, 1/N\}$. The green color shows the background region which does not have any intersection with any training shape. The blue color shows the object region which is the intersection of all projected training shapes.

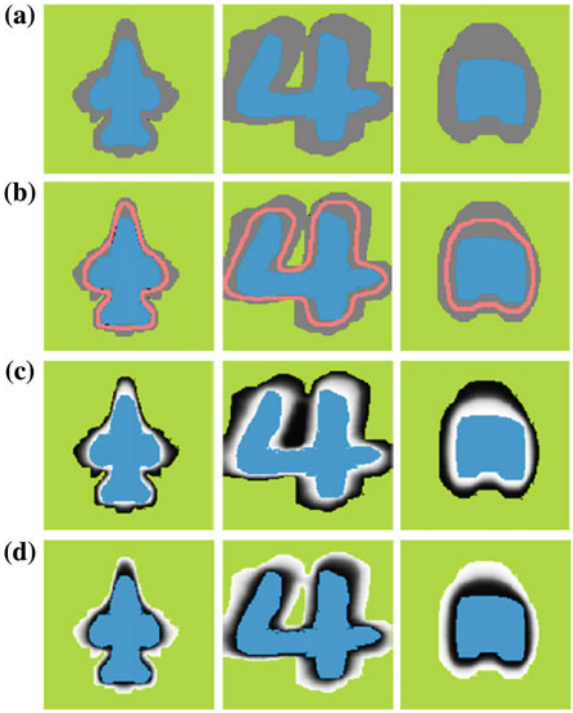

Fig. 6 **a** The *gray* color represents the variability region. **b** The *red* color shows the contour of the average shape (Φ_p). **c** The object (p_o^s) and **d** background (p_b^s) shapes are modeled in the variability region which the pixel values are defined in (0 : 1)

5.1.2 Level Sets Segmentation

The level sets formulation was first introduced by Osher and Sethian [19]. Topology changes like merging and splitting, are handled naturally without the need of parameterization. Given a curve C, it can be embedded into a higher dimension function Φ as $C = \{\mathbf{x} : \Phi(\mathbf{x}) = 0\}$. Then the curve is defined as the zero level of the implicit function. If the time t is added to the function, curve evolution function is changed to $\Phi = \Phi(\mathbf{x}, t)$. The surface function Φ evolves with the time and the evolution front is always represented as the zero level. In the literature, the final level sets formulation is defined as follows:

$$\Phi(t + \Delta t) = \Phi(t) - F|\nabla\Phi|\Delta t = 0 \tag{17}$$

There has been various methods to model the speed function, F. In this paper, a new method which is integrating the intensity and prior shape information is proposed. We use two energy functionals to be minimized. The first functional is to extract object regions using image intensities only with a statistical level set evolution as

described in [22]. We need this step to obtain the image feature to be used in the shape registration process. The second functional, which is slightly different than the formulation proposed in [26], depends on the dissimilarity measure between our shape model and the resulting contour which is obtained in the first phase.

The data is assumed to consist of two classes: object and background. Suppose that the intensity probability density function (*pdf*) within each of these two regions, denoted as p_o^I and p_b^I, can be modeled using a Gaussian distribution whose parameters are adaptively updated during the course of evolution ofthe level set function. The segmentation process starts by initializing the level set function as the signed distance function of a circle centered at a seed point(s) that is placed automatically using the Matched filter [31] or with manual annotation. Then, the statistical parameters corresponding to the *pdf* for the object and background are estimated as follows:

$$\mu_o = \frac{\int_\Omega I(\mathrm{X})H(-\Phi_{\mathbf{f}^*})d\Omega}{\int_\Omega H(-\Phi_{\mathbf{f}^*})d\Omega}, \quad \mu_b = \frac{\int_\Omega I(\mathrm{X})H(\Phi_{\mathbf{f}^*})d\Omega}{\int_\Omega H(\Phi_{\mathbf{f}^*})d\Omega},$$

$$\sigma_o^2 = \frac{\int_\Omega (I(\mathrm{X}) - \mu_o)^2 H(-\Phi_{\mathbf{f}^*})d\Omega}{\int_\Omega H(-\Phi_{\mathbf{f}^*})d\Omega}, \quad \sigma_b^2 = \frac{\int_\Omega (I(\mathrm{X}) - \mu_b)^2 H(\Phi_{\mathbf{f}^*})d\Omega}{\int_\Omega H(\Phi_{\mathbf{f}^*})d\Omega},$$

$$\pi_o = \frac{\int_\Omega H(-\Phi_{\mathbf{f}^*})d\Omega}{\int_\Omega d\Omega}, \textit{and} \quad \pi_b = \frac{\int_\Omega H(\Phi_{\mathbf{f}^*})d\Omega}{\int_\Omega d\Omega} \tag{18}$$

where μ, σ, and π are the mean, standard deviation, and prior probability of the corresponding *pdf* [22]. Object and background regions are represented by $H(-\Phi)H(\Phi)$, respectively. The pixel position, (x, y), is represented as $(\mathbf{x})$. The intensity based energy term is modeled to maximize posterior probability of each region as follows:

$$E_{intensity}(\Phi_{\mathbf{f}^*}) = -\int_\Omega P_o^I(I(x))H(-\Phi_{\mathbf{f}^*})d\Omega - \int_\Omega P_b^I(I(x))H(-\Phi_{\mathbf{f}^*})d\Omega + \in L, \tag{19}$$

where L is the front length of the surface area and $\in$ is a constant between 0 and 1. The change of the level set function with time is calculated by the Euler-Lagrange with the gradient descent given as:

$$\frac{\partial \Phi_{\mathbf{f}^*}}{\partial t} = -\frac{\partial E_{intensity}}{\partial \Phi_{\mathbf{f}}^*} = \delta(\Phi_{\mathbf{f}^*})[P_0^I(I(x)) - P_b^I(I(x))] + \in K \tag{20}$$

where k is the curvature of the evolving contour (or derivative of L) and δ is the derivative of the Heaviside step function. By solving this gradient descent formulation, the initial segmented region $(\Phi_{\mathbf{f}^*})$ is obtained. After this step, the shape energy (E_{shape}) is optimized using the shape based functions which are defined in Eqs. 15 and 16.

After the object region is initially segmented, the shape model is embedded into this domain by minimizing the new energy functional. It should be noted that the method is implemented in 2D dimension in this work. However, the extension of 3D

dimension is straightforward. A transformation matrix, **T**, that gives pixel-wise correspondences between the two shape representations Φ_{source} and Φ_{target} is required. The transformation has scaling, rotation, and translation components represented as follows:

$$S = \begin{bmatrix} s_x & 0 \\ 0 & s_y \end{bmatrix}, R = \begin{bmatrix} \cos(\theta) & -\sin(\theta) \\ \sin(\theta) & \cos(\theta) \end{bmatrix}, Tr = [t_x, t_y]^t. \tag{21}$$

The transformation will be in the form of $\boldsymbol{T(x)} = \boldsymbol{X} = \boldsymbol{SRx} + Tr$ where $\boldsymbol{X} \in \Phi_{\mathbf{f}^*}$ and $\boldsymbol{x} \in \Phi_{\mathbf{P}}$ The proposed dissimilarity measure is

$$E_{shape}(\Phi) = \rho E_{Global} + E_{Local}, \tag{22}$$

where ρ is the normalization constant which controls the relationship between the first and second terms which can be described as follows:

$$E_{Global}(\Phi_{\mathbf{P}}, \Phi_{\mathbf{f}^*}|T) = \int_{\Omega} (\sqrt{s_x s_y}\Phi_{\mathbf{P}}(x) - \Phi_{\mathbf{f}^*}(X))^2 d\Omega, \tag{23}$$

$$E_{Local}(\Phi_{\mathbf{f}^*}, P_{o,b}^{S,I}|W) = -\int_{\Omega} P_o^S(x) P_o^I(x) H(-\Phi_{\mathbf{f}^*}(x)) d\Omega \; - \int_{\Omega} P_b^S(x) P_b^I(x) H(\Phi_{\mathbf{f}^*}(X)) d\Omega. \tag{24}$$

The first term of the proposed energy formulation is the (sum-of-squared distance) SSD of matched distances. It helps to estimate the registration parameters $(s_x, s_y, \theta, t_x, t_y)$, iteratively. Distance changes anisotropically in x-y directions. That's why the geometric mean between s_x and s_y as an approximation is proposed, since the SDF is not invariant to inhomogeneous scaling. After the registration parameters are estimated the shape model, Φ_p, and the projected training shapes, $\{\Phi_1^t, \ldots, \Phi_N^t\}$, are registered to the target domain using the affine transformation. However, this approximation still may not be enough to perfectly align the shapes. Hence, it is needed to add the other shape *pdf* term. A pixel inside the object of interest needs to have bigger object probability. At the same time, this pixel needs to have smaller background probability as well. So, the second term maximizes the probability for object pixels to be correctly classified as internal points. The same will happen for the background points. This step helps to estimate the shape weighting coefficients ($\mathbf{w} = \omega_1, \ldots, \omega_N$) and to refine the result of the first component more accurately. Our proposed framework including the training step is shown in Fig. 7. The registration and weighting parameters $(s_x, s_y, \theta, t_x, t_y, \omega_1, \ldots, \omega_N)$ are computed to minimize E_{shape} using the Nelder-Mead simplex optimization method which was first proposed by Nelder and Mead and proved using theoretical results by Lagarias et al. [32]. The Nedler-Mead method aims to minimize a scalar-valued nonlinear function of n variables using function values, hence it is one of the direct search methods.

5.2 Evaluation

To assess the accuracy and robustness of our proposed framework, we tested it using clinical data sets as well as synthetic and phantom images. All algorithms are implemented on a PC with a 3 GHz AMD Athlon 64 × 2 Dual processor, with 3 GB RAM. First, we describe the experimental results on synthetic images. Second, validation on the European Spine Phantom (ESP) with various noise levels and clinical data sets will be shown. Effect of initialization will be evaluated.Shape based segmentation is useful when the target shape has some occlusions and missing information.

5.2.1 Shape-Based Segmentation of Synthetic Objects

Figures 8 and 9 show results on synthetic jet airplane and number four images with some missing information or occlusions. As seen in the results, the first component (of Eq. 22) is useful for an approximate transformation of the shape model. The second component enhances the segmentation with updated shape coefficients. Hence, the proposed dissimilarity measure is able to improve the global registration results. The results show that occlusions and missing information mislead those methods based only on intensity model. Using the shape prior information the desired shapes are recovered. Also, we observe that the proposed method slightly improves segmentation quality of our previous study [27]. As shown in Fig. 8. The proposed method is more able to capture the fine details and corners of the objects.

In [11, 24], the dissimilarity measures have limitations to capture the object-of-interest if the source and target shapes have inhomogeneous scale differences. Figure 10 shows the results when the target shapes have (i) homogeneous, and (ii–iv) inhomogeneous scale differences. Because dissimilarity measures of two alternative methods discard a possible scale difference in x or y directions, they fail when the target shapes are scaled inhomogeneities in x-y directions. The results prove that the proposed method overcomes the problems inhomogeneous scale differences. The computational costs of the two alternative methods [11, 24] and our method on 40 images (with 128 × 128 size) are approximately 220, 340, and 360 s, respectively. Since the method described in [11] does not estimate the shape coefficients in the optimization, it executes the experiment in faster time. Also, since the proposed method estimates two scaling parameters (s_x, s_y), the execution time may be expected to be slightly higher than other two alternatives.

5.2.2 Shape-Based Segmentation of Vertebral Body from CT

Our approach is also tested on clinical CT images to segment vertebral bodies (VBs) as well as the European spinal phantom (ESP). The vertebra consists of the VB and spinal processes. The red color shows the contour of the region of interest in Fig. 11. The objective is to segment the VB region correctly. Spinal processes and ribs should

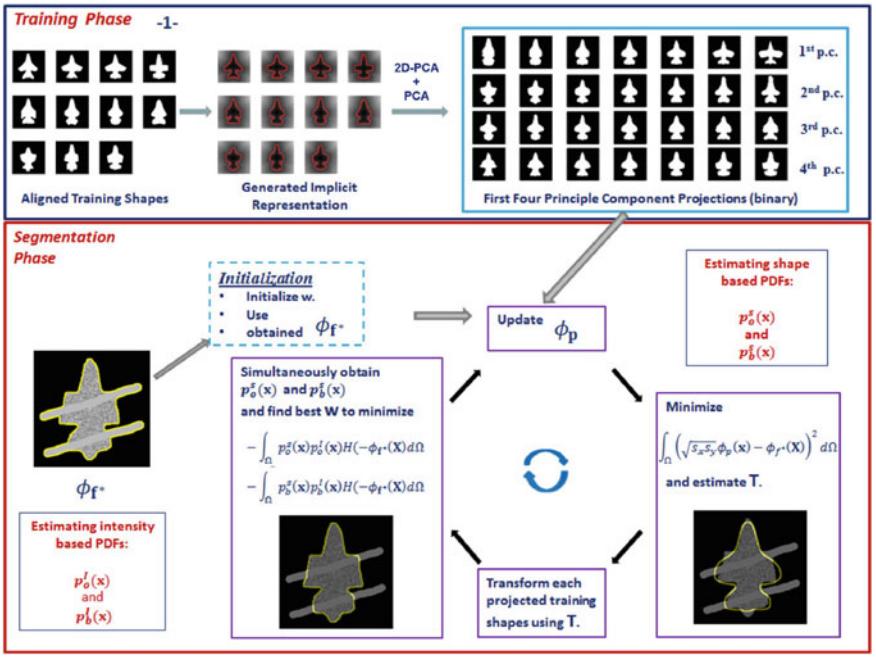

Fig. 7 The general framework is shown. The steps can listed as follows: *1* Obtain shape projections to define the shape variability. *2* Segmentation

not be included in the bone mineral density (BMD) measurements. The clinical data sets were scanned at 120 KV and 2.5 mm slice thickness. In this experiment, 260 testing CT slices (totals to 15 VBs) which are obtained from 13 different patients and different spine bone regions (i.e. lumbar, thoracic, etc.) are tested. To assess the proposed method under various challenges, a zero mean Gaussian noise was added to the CT images with different signal-to-noise ratios (SNR). To compare the proposed method with other alternatives, VBs are subsequently segmented using two other methods; (1) the active appearance model (AAM) [23], and (2) our earlier PCA-based approach which is described in [8].

Segmentation accuracy is measured for each method using the ground truths (expert segmentation). To evaluate the results, the percentage segmentation accuracy (A) is calculated as follows:

$$Dice's\ Coefficient(A\%) = \frac{100 * 2TP}{2TP + FP + FN}. \tag{25}$$

where TP is the number of true positives, FP is the number of false positives, and FN is the number of false negatives. The segmentation accuracy is shown in Table 2. It is clear that the noise immunity of our method are much higher than other alternatives. Figure 11 shows the segmentation results of the proposed framework with different scaling, translation, and rotation initializations.

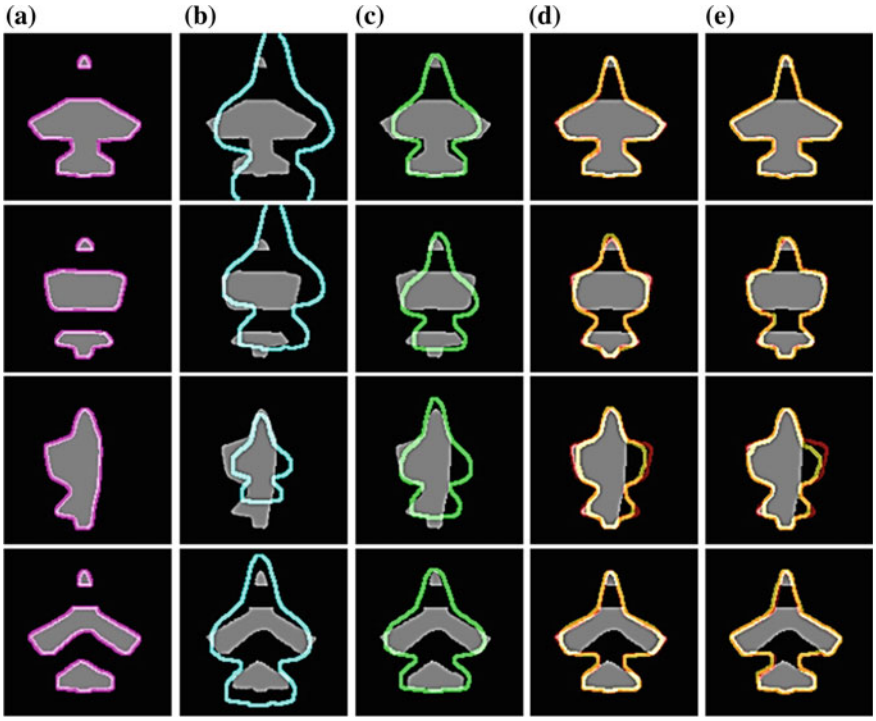

Fig. 8 Segmentation results of a synthetic jet airplane images with different missing information and initializations. **a** The intensity only based segmentation results. **b** Different shape model initialization. **c** The results using only the first term of Eq. 22. **d** [27]. **e** The segmentation of the proposed method (the *red*and *yellow* colors show the contour of the ground truth shape region, and the contour of the automatically segmented region, respectively)

Table 2 Average segmentation accuracy of the proposed vb segmentation on 272 ct images. The size of each image is 512 × 512

	$SNR = 100\,dB$	$SNR = 50\,dB$	$SNR = 10\,dB$	$SNR = 1\,dB$	s/slice
Intensity based, %	79.3	66.2	57.9	51.8	5.6
AAM [23], %	85.2	83.7	79.0	76.1	7.2
PCA-based [8], %	89.3	83.6	81.8	81.3	10.8
Proposed, %	94.3	92.9	89.3	86.8	11.3

Results indicate that the performance of our method is almost constant with different initialization parameters. To quantitatively demonstrate the accuracy of our approach, we calculate the average segmentation accuracy of our segmentation method on 272 CT images (including 12 ESP images) the under various signal-to-noise ratios and compare the results with the two other methods (Intensity-based and PCA-based). Our 2D-PCA based framework outperforms the conventional PCA described in [8] as shown in Fig. 12a.

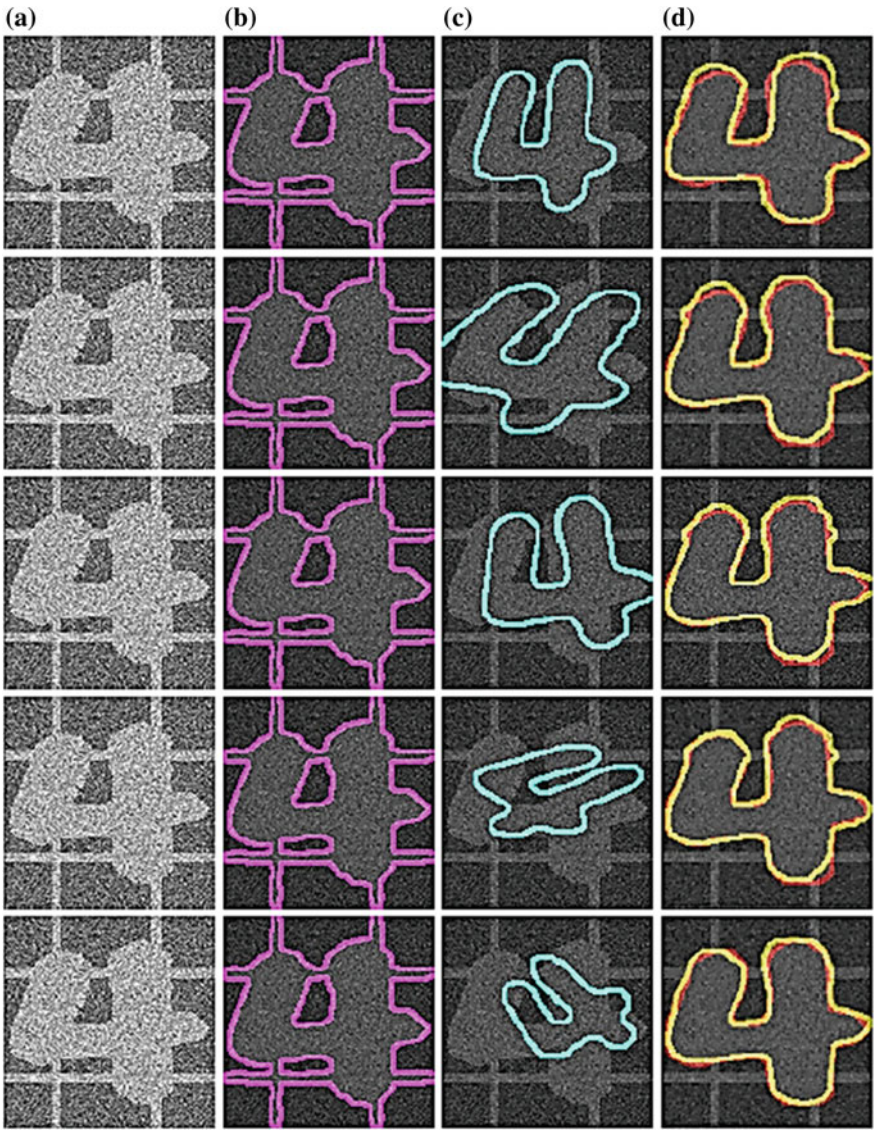

Fig. 9 Segmentation results on a synthetic number "4" with occlusions and different shape initializations. **a** the image with occlusions and noise. **b** the segmentation results using intensity only information. **c** different shape model initializations. **d** the result of the proposed method (the *red* and *yellow* colors show the contour of the ground truth shape region, and the contour of the automatically segmented region, respectively)

Additionally, Fig. 12b studies the effect of choosing the number of the projected training shapes N (by changing the chosen value of L) on the segmentation accuracy. From this figure, we can conclude that the performance of 2D-PCA is better than

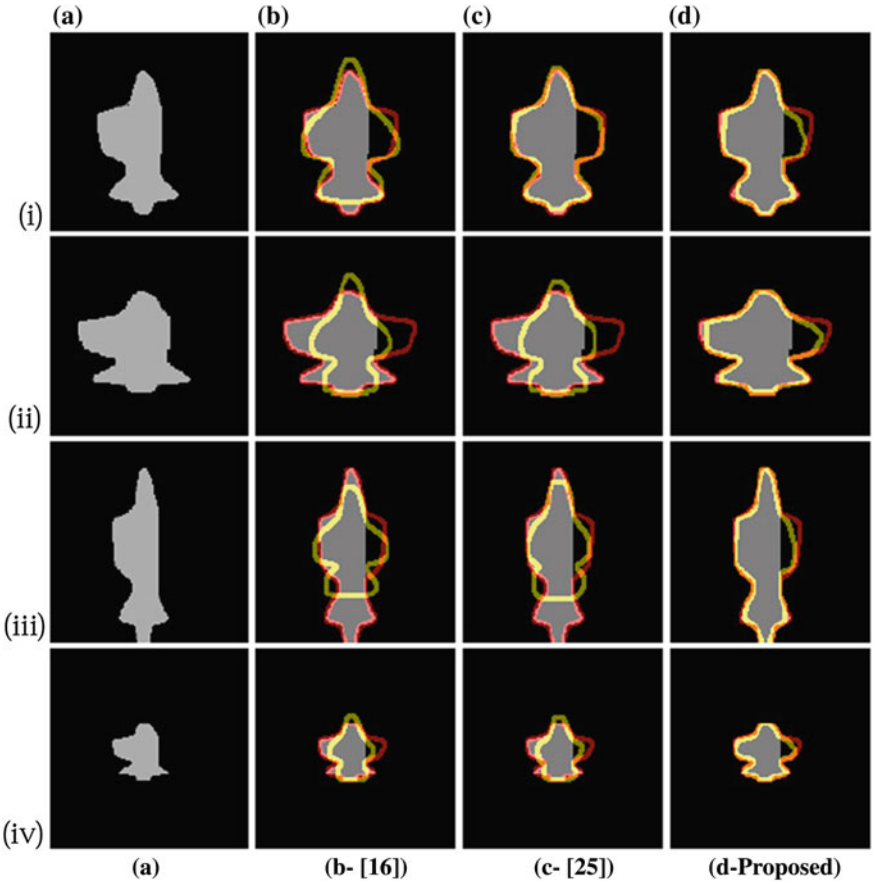

Fig. 10 Comparison with two closest works described in [11, 24]. Testing shapes with (**i**) homogeneous and (**ii**–**iv**) inhomogeneous scaling factors. (i) sx = 1.0, sy = 1.0, (ii) sx = 0.7 sy = 1.3, (iii) sx = 1.2, sy = 0.7, (iv) sx = 0.4, sy = 0.7 (the *red* and *yellow* colors show the contour of the ground truth shape region, and the contour of the automatically segmented region, respectively

the conventional PCA under the same number of training shapes. In other words, to get the same accuracy of PCA framework, the 2D-PCA needs fewer training shapes. Using the shape model, the spinal processes are eliminated automatically without any computational cost and execution time. This contribution is very important for the BMD measurements which are restricted to the VBs.

6 Summary and Possible Extensions

This chapter considered elastic registration of shapes and its applications in the segmentation problem. Shape representation was performed using the vector distance function (VDF). The energy function for global and local registrations was described.

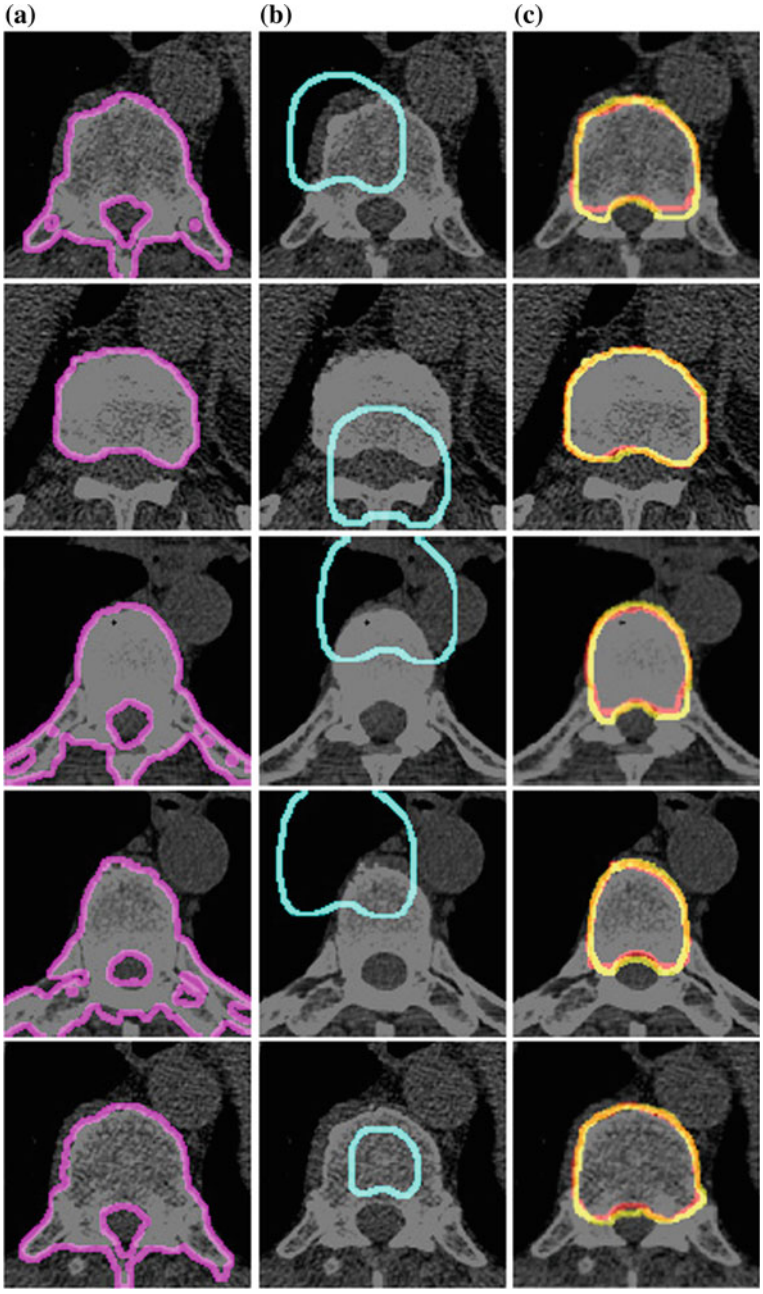

Fig. 11 Segmentation results of clinical CT images. **a** intensity only based segmentation results. **b** different initialization of the shape model. **c** the proposed segmentation results (the *red* color shows the contour of the ground truth shape region, the *yellow* color shows the contour of the automatically segmented region)

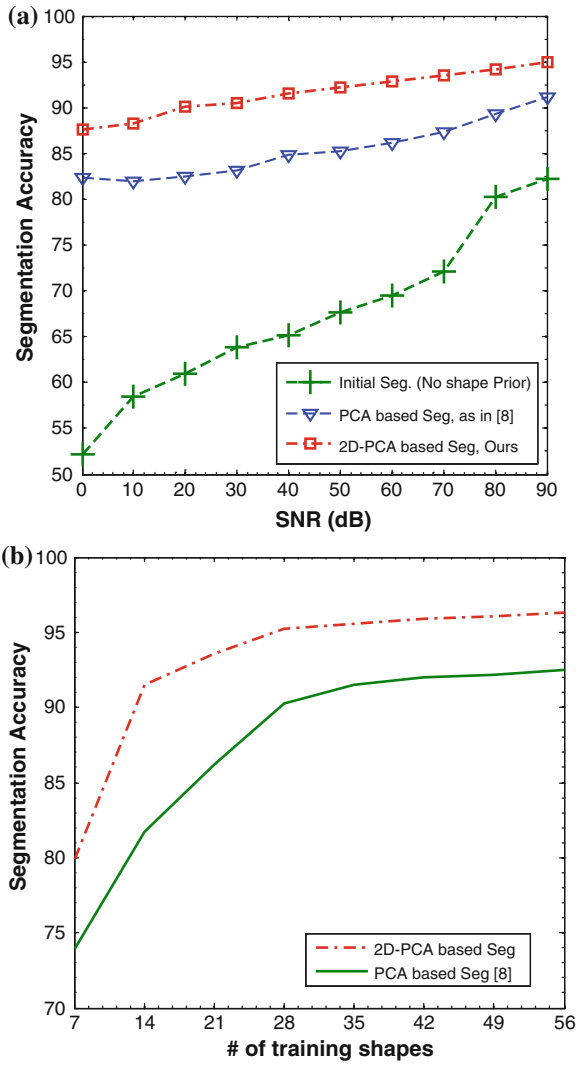

Fig. 12 **a** the average segmentation accuracy of different segmentation methods on 272 CT images under various signal-to-noise ratios. **b** the effect of choosing the number of the projected training shapes N on the segmentation accuracy

Creating a shape prior was studied for a number of examples. We have demonstrated the registration problem by matching vector implicit spaces representation of shapes. We formulated the process as an energy minimization problem. Gradient descent is used for optimizing the global registration energy with proper initialization of the transformation parameters.

The use of vector implicit representation helps generalize the global transformation and hence, results are improved. In local registration, the situation is different because the number of unknown parameters used to represent deformations is large. Gradient descent is an awkward step in this situation. We adopt a closed form solution for the elastic registration problem by formulating a quadratic function, which leads to a convex optimization system. The proposed approach avoids using large number of iterations required for the minimization by gradient descent optimization. We demonstrated several experimental results for synthetic and real shape registration cases. The proposed approach is competitive when compared to the state of the art techniques. Qualitative, quantitative, and comparative experimental results have been demonstrated for both global and local registration cases. An application for nodular region segmentation has been illustrated to assure that the proposed technique has a wide range of applications. Regarding future directions, the proposed approach can be implemented in 3D in a straightforward manner, which will help in applications like 3D face recognition.

References

1. Abd El Munim H, Farag AA (2007) Shape representation and registration using vector distance functions. In: Proceedings of IEEE conference on computer vision and pattern recognition (CVPR'07), Minneapolis, MN, June 18–23 2007
2. Abd EL Munim H, Farag AA (2007) Curve/surface representation and evolution using vector level sets with application to the shape-based segmentation problem. IEEE Trans Pattern Anal Mach Intell 29(6):945–958
3. Abd El Munim HE, Farag AA (2007) A new global registration approach of medical imaging using vector maps. In: Proceedings of international symposium on biomedical imaging, ISBI'07, Metro Washington DC, pp 584–587, April 12–15 2007
4. Abd El Munim HE, Farag AA (2007) A new variational approach for 3D shape registration. In: Proceedings of international symposium on biomedical imaging, ISBI'07, Metro Washington DC, pp 1324–1327, April 12–15 2007
5. Fahmi R, Farag AA (2008) A fast level set algorithm for shape-based segmentation with multiple selective priors. In: Proceedings of IEEE international conference on image processing (ICIP'08), San Diego, California, Oct 12–15 2008
6. Farag A, Abdelmunim H, Graham J, Farag AA, Elshazly S, Ali AM, Farag A, Al Mogy S, Al Mogy M, Falk R, Al Jafary S, Mahdi H, Milam R (2011) Variational approaches for segmentation of lung nodules. IEEE international conference on image processing (ICIP), pp 2157–2160, Sept 2011
7. Aslan MS, Ali A, Farag AA, Abdelmunim H, Arnold B, Xiang P (2011) A new segmentation and registration approach for vertebral body analysis. In: Proceedings of 2011 IEEE international symposium on biomedical imaging (ISBI), pp 2006–2009, March 2011
8. Aslan MS, Mustafa E, Abdelmunim H, Shalaby A, Farag AA, Arnold B (2011) A novel probabilistic simultaneous segmentation and registration using level set. In: Proceedings of 2011 IEEE international conference on image processing (ICIP), pp 2161–2164, Sept 2011
9. Abdelmunim H, Farag AA (2011) Elastic shape registration using an incremental free form deformation approach with the ICP algorithm. In: Eighth Canadian conference on computer and robot vision (CRV), pp 212–218, May 2011

10. Abd El Munim HE, Farag AA, Farag AA (2013) Shape representation and registration in vector implicit spaces: adopting a closed form solution in the optimization process. In: IEEE Transactions on Pattern Analysis and Machine Intelligence PAMI'13, March 2013
11. Paragios N, Rousson M, Ramesh V (2002) Matching distance functions: a shape-to-area variational approach for global-to-local registration. In: European conference in computer vision. Denmark, Copenhagen, June 2002
12. Xie Z, Farin GE (2004) Image registration using hierarchical B-splines. IEEE Trans Visual Comput Graphics 10(1):85–94
13. Sederberg T, Parry S (1986) Free-form deformation of solid geometric models. In: ACM SIGGRAPH, pp 151–160
14. Rueckert D, Sonoda L, Hayes C, Hill D, Leach M, Hawkes D (1999) Nonrigid registration using free-form seformations: application to rreast MR images. IEEE Trans Med Imaging 8:712–721
15. Huang X, Paragios N, Metaxas DN (2006) Shape registration in implicit spaces using information theory and free form deformations. IEEE Trans PAMI 28(8):1303–1318
16. Diciotti S, Lombardo S, Falchini M, Picozzi G, Mascalchi M (2011) Automated segmentation refinement of small lung nodules in CT scans by local shape analysis. IEEE Trans Biomed Eng 58(12):3418–3428
17. Besl P, Mckay N (1992) A method for registration of 3-D shapes. IEEE Trans PAMI, 14(2):239–256
18. Kendall DG (1989) A survey of the statistical theory of shape. Stat Sci 4(2):87–120
19. Osher S, Sethian JA (1988) Fronts propogating with curvature-dependent speed: algorithms based on Hamilton-Jacobi formulations. J Comput Phys 79:12–49
20. Kass M, Witkin A, Terzopoulos D (1988) Snakes: active contour models. Int J Comput Vis 1(4):321331
21. Chan TF, Vese LA (2001) Active contours without edges. IEEE Trans Image Process 10(2):266277
22. Farag AA, Hassan H (2004) Adaptive segmentation of multi-modal 3D data using robust level set techniques. In: Proceedings of international conference on medical image computing and computer-assisted intervention (MICCAI'04), pp 143–150
23. Cootes TF, Taylor CJ, Cooper DH, Graham J (1995) Active shape models—their training and application. Comput Vis Image Understanding 61:38–51
24. Tsai A, Yezzi A, Wells W, Tempany C, Tucker D, Fan A, Grimson WE, Willsky A (2003) A shape-based approach to the segmentation of medical imagery using level sets. IEEE Trans Med Imaging 22(2):137–154
25. Taron M, Paragios N, Jolly MP (2007) Registration with uncertainties and statistical modelling of shapes with variabile metric kernels. IEEE Trans Pattern Anal Mach Intell 1(8):1–14
26. Cremers D, Osher SJ, Soatto S (2006) Kernel density estimation and intrinsic alignment for shape priors in level set segmentation. Int J Comput Vision 69(3):335–351
27. Aslan MS, Abdelmunim H, Farag AA (2011) A probabilistic shape-based segmentation using level sets. In: First IEEE workshop on information theory in computer vision and pattern recognition (ICCV workshop)
28. Mahmoodi S (2009) Shape-based active contours for fast video segmentation. IEEE Trans Signal Process Lett 16(10):857–860
29. Mumford D, Shah J (1989) Optimal approximations by piecewise smooth functions and associated variational problems. Xommun Pure Appl Math 42(4):577–688
30. Shalaby A, Aslan M, Abdelmunim H, Farag AA (2012) 2D-PCA based shape prior for level sets segmentation framework of the vertebral body. In: Proceedings of the 6th Cairo international conference on biomedical engineering (CIBEC'12), Cairo, Egypt, pp 134–137, Dec 22–25 2012
31. Kumar BVKV, Savvides M, Xie C (2006) Correlation pattern recognition for face recognition. Proc IEEE 94(11):1963–1976
32. Lagarias JC, Reeds JA, Wright MH, Wright PE (1998) Convergence properties of the nelder-mead simplex method in low dimensions. SIAM J Optim 9(1):112–147